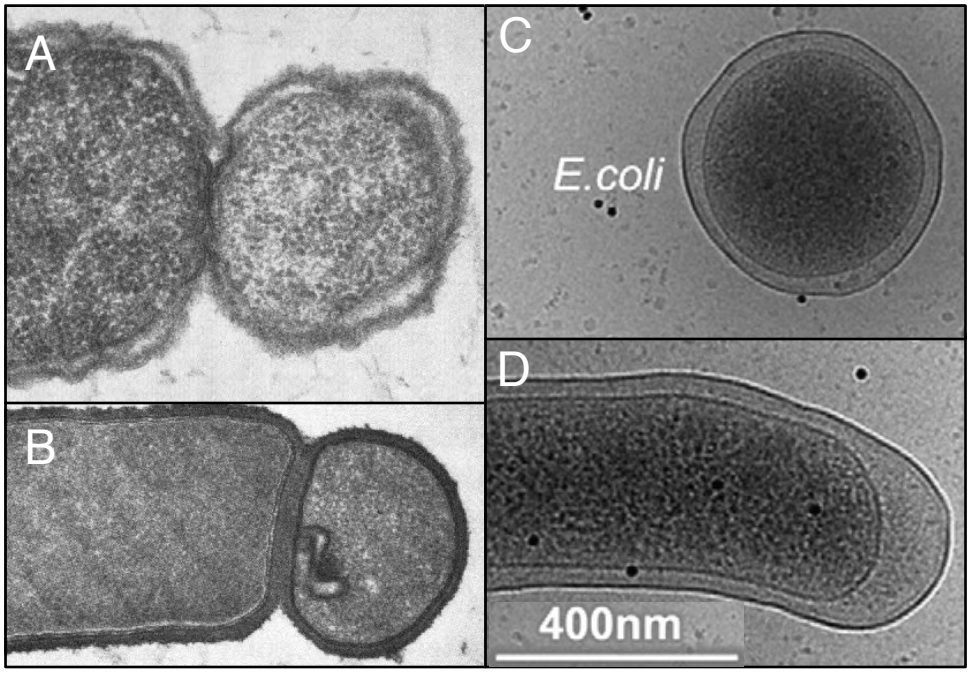

Fig. 1. Micrographs of minicell producing cells. Electron micrograph of a thin section of an *E. coli* **(A)** and *B. subtilis* **(B)** parental cells producing a minicell by division at a polar septum. Cryo-ET micrograph of an *E. coli* tiny minicell **(C)** and a parental rod shaped skinny cell **(D)**. Figure was adapted from references (12) and (17).

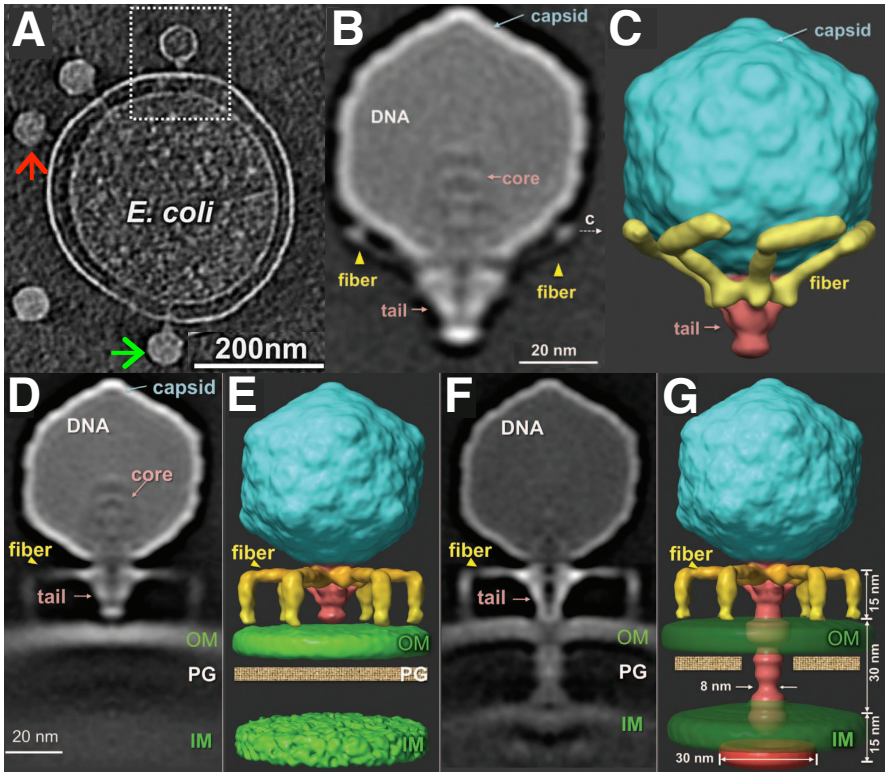

Fig. 2. Cryo-ET tomograms of cross-sectional view perpendicular to the cell envelope of T7 phage associating with *E. Coli* minicells **(A)** and subvolume averaging reconstructions depicting cross section and 3D surface renderings of non-cell associated **(B and C)** and cell attached **(D - G)** T7 phage. **(A)** T7 phage are seen at various stages of the infection process. The T7 particle emphasized by the red arrow depicts the first stage of infections where the phage is attached but a DNA translocation structure is not yet elaborated. The T7 particle emphasized by the green arrow is at the second stage of infection where the internal core proteins have elaborated a tail structure that protrudes through the cellular envelope but has not yet translocated DNA. The T7 particle emphasized by the white box is at the final stage of infection where image densities in the capsid are gone, indicating the translocation of DNA. **(B and C)** Asymmetrical reconstructions derived from 6116 subvolumes revealing tail fibers pointing up and wrapped around head. **(D and E)** Symmetrical reconstruction of subvolumes of 3352 T7 phage bound to the cell surface by attachment of tail fibers but before tail tube elaboration. **(C and D)** Symmetrical reconstruction of subvolumes of 1886 T7 phage bound to the cell surface after elaboration of the tail tube but before injection of the phage genome into the cell. Figure was adapted from reference (18).

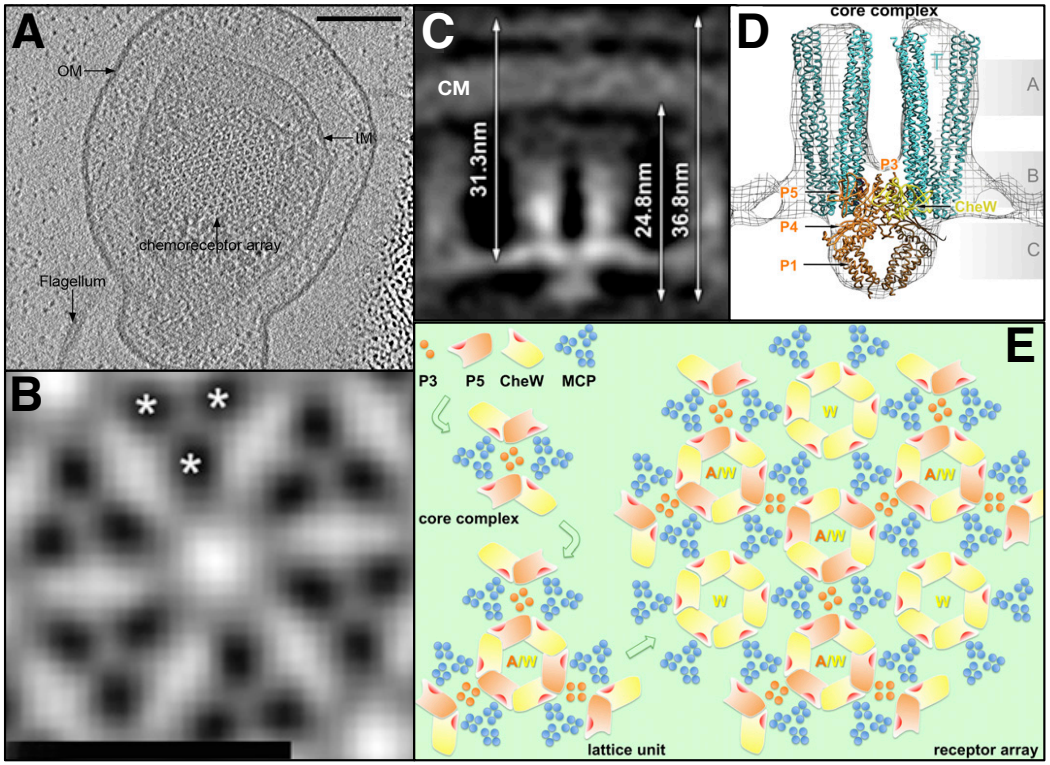

Fig. 3. Cryo-ET tomographs of: a cross-sectional view parallel to the cell membrane of an *S. enterica* minicell chemotaxis receptor array **(A)** OM: outter membrane : IM: inner membrane.(Scale bar: 100 nm) **(B)** Subvolume averaged reconstruction of hexagonal array unit of *S. enterica* chemoreceptor; each white asterisk emphasizes an MCP functional unit. (Scale bar: 12 nm) **(C)** Subvolume averaged reconstruction of a cross-sectional view perpendicular to the cytoplasmic membrane (CM) of *E. coli* minicell depicting MCP chemoreceptor trimer pillars (green arrows) and CheA/W baseplate (red arrow). **(D)** 3D density map (derived from subvolume averaged tomographs) of a perpendicular cross-sectional view of *E. coli* minicell. An atomic model of the cytosolic portion of MCP chemoreceptors trimer pillars (teal colored ribbon model) is docked into the corresponding density and continues into density regions that correspond to the CheA/W baseplate. The atomic models of CheW (yellow colored ribbon model) and the P1, P3, P4 and P5 domains of CheA (orange colored ribbon model) are docked into their corresponding densities adjacent to the cytosolic end of the MPC pillar structures. **(E)** Cartoon model illustrating the organization and molecular interactions that mediate the assembly of a chemoreceptor array composed of multiple hexagonal lattice units.

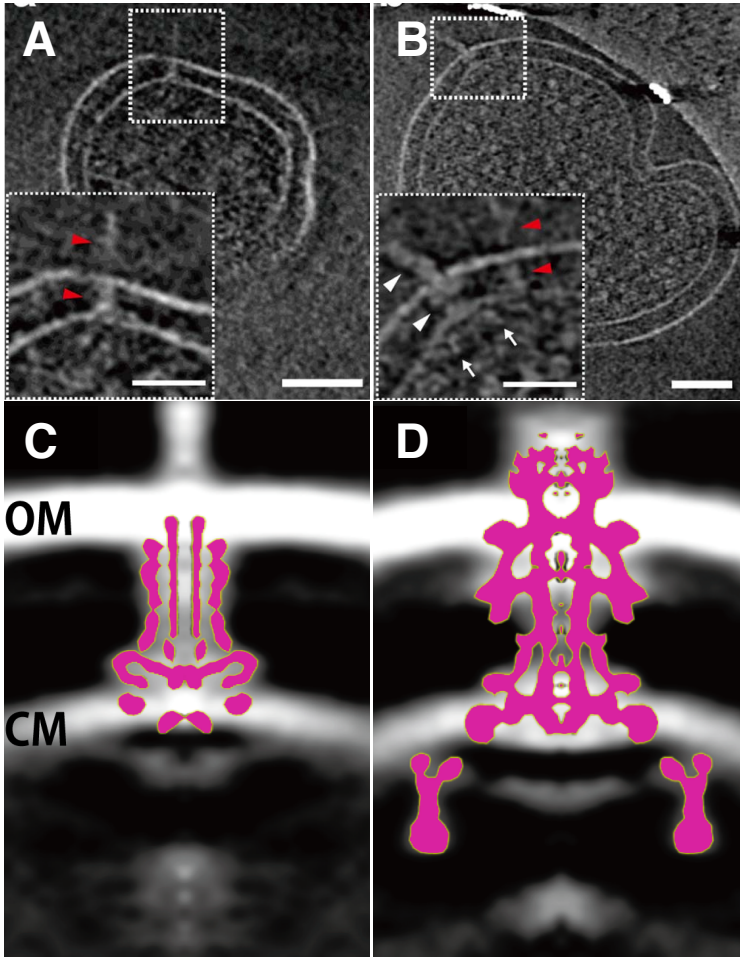

Fig. 4. Cryo-ET tomograms and subvolume average reconstructions of cross-sectional views perpendicular to the cell envelope of the T3S injectosome **(A and C)** and flagellar body **(B and D)** elaborated in *S. enterica* minicells. **(A and B)** The injectosome and flagellar body is emphasized by white boxes in the unmagnified images depicting whole minicells. (Scale bar: 100 nm) In the embedded magnified images (Scale bar: 50 nm): **(A)** the red arrow at the top emphasizes the needle complex while the lower emphasizes the multi-ring basal body transversing the periplasm; **(B)** the larger white arrows closer to the left border emphasize the extracellular flagella (top) and the multi-ring basal body transversing the periplasm (bottom). The two smaller white arrows over the cytoplasmic region emphasize the cytoplasmic basal body. **(C and D)** Density map reconstruction with a superimposed cartoon figure (colored pink) of the injectosome and flagellar body structures (respectively) generated from isolated T3S machines. **(C)** Comparison between in the in situ density map and the cartoon figure shows that the structural elements of the multiring basal complex is conserved in isolated injectosomes but other components such as the needle complex and the cytoplasmic basal body is absent as depicted by image densities present in the cytoplasmic and extracellular regions. **(D)** Comparison between the in situ density map and the cartoon figure show that the multiring basal body and a cytosolic structure, the C-ring are conserved in isolated flagellar bodies but that other uncharacterized cytosolic structures (for extracellular flagellar systems) are observed as depicted by image densities in the cytosol. **(C and D)** Comparison between both T3SSs revealed that the multi-ring basal body of injectosome systems is much simpler and smaller than the flagellar system. OM: outer membrane; IM: inner membrane.

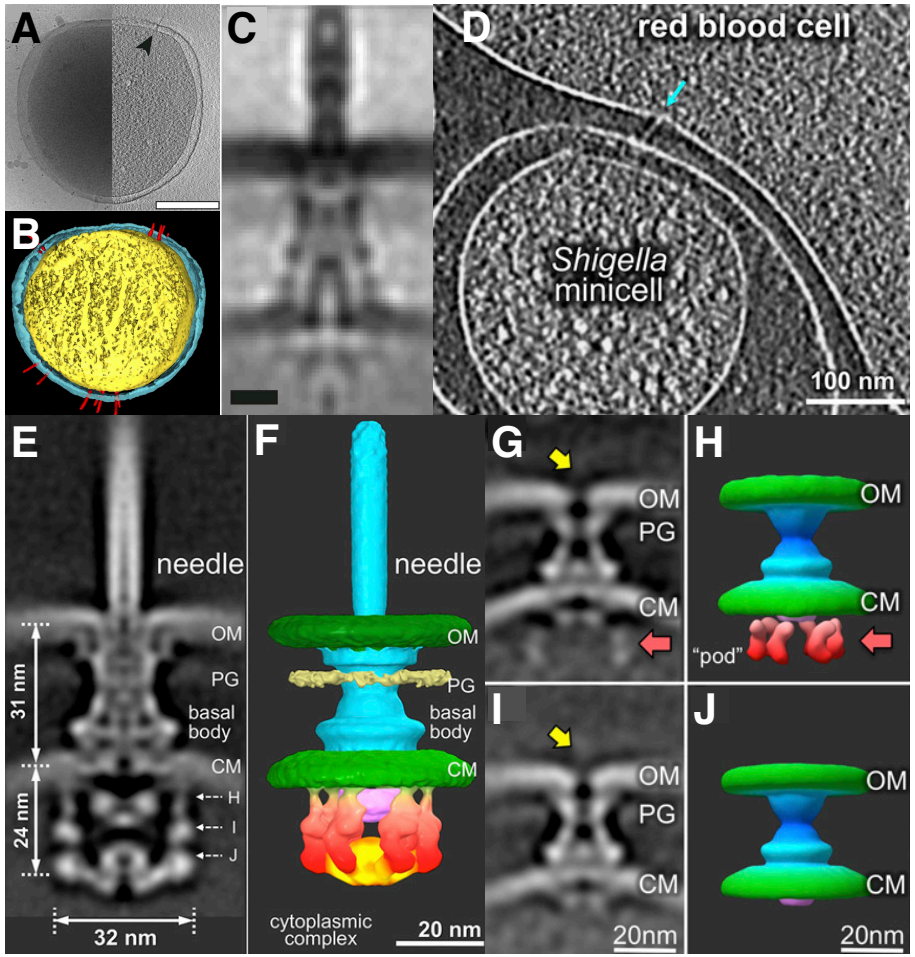

Fig. 5. Cryo-ET tomogram **(A)** and 3D volume rendering **(B)** of *Y. enterocolitic* minicell with elaborated T3S injectosome.